Desalination 637 (2026) 120500

Contents lists available at ScienceDirect

Desalination

journal homepage: www.elsevier.com/locate/desal

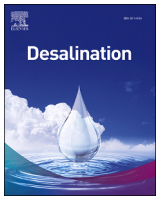

Activation of peroxydisulfate by Cu single-atom catalysts for efficient bisphenol A degradation

Xueyang Fan [a,c,1], Yuxuan Zhang [a,1], Zhenjun Tian [a], Shengwang Gao [a,b,*], Caili Du [a], Yangwei Bai [a], Lieyu Zhang [a,**]

[a] State Key Laboratory of Environmental Criteria and Risk Assessment, State Environmental Protection Key Laboratory of Estuarine and Coastal Environment, Chinese Research Academy of Environmental Sciences, Beijing, 100012, China
[b] College of Water Sciences, Beijing Normal University Beijing, 100875, China
[c] School of Resource & Environment and Safety Engineering, University of South China, Hengyang, 421001, China

HIGHLIGHTS

- N-HCMS@CuSA achieved 100% BPA degradation in 12 min with an ultra-low dosage.
- Cu-N_4 sites triggered a highly selective direct electron transfer (DET) pathway.
- GOS and DFT quantitatively linked degradation rates to half-wave potentials.
- The DET regime ensured exceptional resistance to humic acid and real wastewater.

GRAPHICAL ABSTRACT

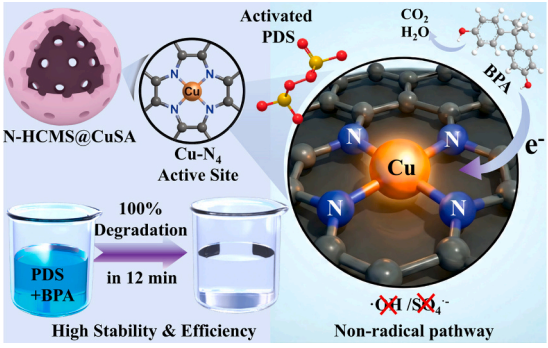

ARTICLE INFO

Keywords:
Peroxydisulfate activation
Copper single atom catalysts
Bisphenol A
Direct electron transfer

ABSTRACT

In advanced oxidation processes based on peroxydisulfate (PDS) activation, establishing a highly selective direct electron transfer (DET) pathway in complex water matrices remains a critical scientific bottleneck. Herein, a hollow mesoporous carbon-anchored Cu single-atom catalyst (N-HCMS@CuSA) was developed for PDS activation, which selectively undergone direct electron transfer pathway and exhibited exceptional intrinsic activity for organic pollutants degradation. The system of N-HCMS@CuSA /PDS achieved 100% degradation of bisphenol A (BPA) within 12 min at an ultra-low catalyst dosage of 0.125 g/L, delivering a turnover frequency (TOF) of 4.90 min^{-1}. A quantitative correlation was established between the reaction rates (k_{obs}) and the half-wave potentials ($\varphi_{1/2}$) of pollutants. Electrochemical analysis, EPR, and radical scavenging experiments revealed that a direct electron transfer (DET) mechanism overwhelmingly dominated the BPA degradation. The construction of a galvanic oxidation system (GOS) provided direct evidence for the interfacial electron flow from BPA to PDS. DFT calculations revealed that the intrinsic Cu—N_4 sites modulate the electronic structure of copper centers to induce

* Corresponding author at: State Key Laboratory of Environmental Criteria and Risk Assessment, State Environmental Protection Key Laboratory of Estuarine and Coastal Environment, Chinese Research Academy of Environmental Sciences, Beijing, 100012, China.
** Corresponding author.
E-mail addresses: gaosw@craes.org.cn (S. Gao), zhanglieyu@163.com (L. Zhang).
[1] These authors contributed equally to this work.

https://doi.org/10.1016/j.desal.2026.120500
Received 7 May 2026; Received in revised form 17 June 2026; Accepted 29 June 2026
Available online 2 July 2026

effective elongation of the O—O bond in adsorbed PDS, thereby minimizing the energy barrier for electron transfer. The N-HCMS@CuSA/PDS achieved over 90% BPA removal efficiency with low copper leaching (0.01–0.02 mg/L) during 10 h of continuous operation. Ultimately, this work not only provides an efficient strategy for high oxidant utilization but also highlights the immense potential of this uniquely configured DET system as a robust pre-treatment strategy to mitigate organic fouling in membrane-based water reclamation facilities.

1. Introduction

The development of city and industry has driven human civilization and social progress. However, the increasing diversity and complexity of organic pollutants in aquatic environments threaten ecological security and human health. As a typical environmental endocrine disruptor, bisphenol A (BPA) has attracted growing attention for its potential health and environmental hazards. [1,2]. Furthermore, in modern desalination facilities and advanced water reclamation plants, the presence of endocrine-disrupting chemicals (EDCs, such as BPA) in source water poses a critical challenge. These ubiquitous trace organic contaminants not only threaten the safety of the product water but also provoke severe and irreversible organic fouling on reverse osmosis (RO) and nanofiltration (NF) membranes [3]. Conventional pre-treatment strategies often rely on chlorination, which inevitably generates highly toxic halogenated disinfection byproducts. Therefore, developing highly efficient, selective, and non-halogenated advanced oxidation processes (AOPs), such as PDS activation, as an integrated pre-treatment step is of paramount importance for protecting desalination membranes and ensuring intake water quality standards [4]. In recent years, peroxydisulfate(PDS)-based advanced oxidation processes (PDS-AOPs) have attracted significant attention for their high catalytic activity in eliminating recalcitrant organic pollutants in aquatic environments and for their diverse oxidation pathways (both radical and non-radical) [5,6]. This process effectively removed organic contaminants from water by generating reactive oxygen species (ROS), including hydroxyl radicals (•OH), sulfate radicals ($SO_4^{\bullet-}$), and superoxide radicals ($O_2^{\bullet-}$), et al. [7–9]. However, the radicals generally suffer from a short life span and competitive reactions with water matrix substances [10,11]. Interestingly, non-radical pathways involving singlet oxygen ($^1O_2$), electron transfer processes (ETP), and highly valent metals [12,13]exhibit superior resistance to interference with highly selective degradation toward electron-rich pollutants [14–16].

Recent research advances have revealed multiple effective PDS activation pathways, including thermal, ultraviolet, ultrasonication, and catalytic approaches [17–19]. Heterogeneous catalysts were proved for effective activation of PDS [20]. Single-atom catalysts (SACs) with well-defined active sites, controllable electronic structure and significantly increases 100% metal atom utilization efficiency are used for effective PDS activation with generation of reactive species [21–23]. Meng et al. [24] investigated the activation of PDS by Co single atoms for phenolic compound degradation, demonstrating that CoNC-MSi exhibited outstanding degradation, maintaining over 96% phenolic degradation efficiency beyond seven cycles. Metal centers with different coordination configurations can trigger diverse PDS activation pathways, including radical, non-radical, and radical-non-radical synergistic mechanisms [25]. Furthermore, most studies indicated that direct electron transfer(DET) have been confirmed as the dominant mechanisms for SACs activating PDS [26,27].DET possesses three significant advantages: (i) it preferentially acts on groups with high electron density or great oxidizability, leading to highly selective degradation of target pollutants; (ii) maintaining high degradation activity in complex real-world aquatic matrices with high tolerance to radical quenchers like HCO_3^-, Cl^-, and natural organic matter,; and (iii) it mitigates the reliance on non-selective radical pathways, achieving targeted detoxification while inhibiting the formation of toxic byproducts [28].

Recent studies have demonstrated that single-atom catalysts supported on nitrogen-functionalized carbon materials (i.e., M-N-C SACs) exhibit exceptional efficiency and durability in Fenton-like catalysis [29,30]. Unlike iron-, cobalt-, and manganese-based catalysts that readily cleave the O—O bond of PDS to trigger radical pathways, Cu-based catalysts offer distinct mechanistic advantages for non-radical processes [31,32]. Distinct from the Fe-based catalysts that typically trigger the radical-generating cleavage of the O—O bond, the unique d-electron configuration of Cu centers facilitates inner-sphere interaction with PDS, leading to the formation of a reactive surface complex. This unique inner-sphere complexation facilitates the establishment of an efficient electron-conducting bridge, thermodynamically favoring the direct electron transfer (DET) pathway from target pollutants to PDS [33,34]. Inspired by these findings, several Cu-based single-atom catalysts derived from nitrogen-doped carbon materials have been applied in recent years to activate PDS for degrading organic pollutants demonstrating outstanding catalytic performance [35,36]. Pan et al. [37] discovered that the Cu(III) oxidation and electron transfer processes induced by the Cu—N_4 site on the single-atom catalyst dominate pollutant degradation during PDS activation. It is important to note that existing PDS activation systems typically exhibit multiple coexisting pathways, which often participate simultaneously. Such complexity makes it challenging to establish a direct correlation between the dominant pathway and specific structural elements [38]. Models of PDS activation dominated by a single pathway of direct electron transfer (DET) are rarely reported. More importantly, the catalytic efficiency of DET in practical applications is often severely constrained by sluggish interfacial mass transfer and low local pollutant concentrations in bulk solutions. To break through this bottleneck, rational catalytic system construction at the is urgently required.

Herein, we rationally designed a single-atom catalyst with Cu—N_4 moieties anchored on nitrogen-doped mesoporous carbon (N-HCMS@CuSA). The catalyst efficiently activated PDS and promoted the degradation of phenolic compounds. The primary objectives of this study are as follows: (1) To investigate the catalytic performance and practical applicability of the N-HCMS@CuSA/PDS system, particularly under continuous flow conditions; (2) To unveil the non-radical mechanism by establishing a quantitative correlation between the half-wave potentials ($\varphi_{1/2}$) of pollutants and their oxidation rates (k_{obs}); (3) To elucidate the intrinsic active sites and confirm the interfacial electron transfer pathway through DFT calculations; and (4) To assess the degradation pathways and toxicity evolution of BPA. The above findings aim to provide theoretical insights into designing high-performance single-atom catalysts for environmental remediation.

2. Experimental methods

2.1. Synthesis of N-HCMS

Details of the materials are described in Text S1. Ammonia solution (NH_4OH, 0.1 mL, 25 wt%) was combined with deionized water (30 mL) and agitated for over 1 h. To this mixture, 3-aminophenol (0.1 g) was added, and agitation was continued for 30 min. The reaction mixture was then supplemented with formaldehyde solution (0.14 mL) and maintained at 30 °C for a further 30 min with stirring. Finally, the resulting solution was introduced into a mixture of deionized water (50 mL), ethanol (20 mL), and ammonia solution (1 mL, 25 wt%), followed by approximately 5 min of mixing. Following the addition of 0.2 g of

CTAB, 10 mL of TEOS was added. After reacting for 10 h, 35 mL of DMF was introduced to dissolve the oligomers. The product was collected by centrifugation, carbonized under a N_2 atmosphere, and then the silica template was etched with 10 wt% hydrofluoric acid to obtain N-HCMS.

2.2. Synthesis of N-HCMS@CuSA

20 mL of mixture containing Cupric(II) acetylacetonate (0.3 g) and EtOH (99 wt%) was ultrasonically dispersed as the Cu precursor. Subsequently, 0.2 g of the carrier (N-HCMS) was ultrasonically dispersed in deionized water for 1 h. The prepared dispersion and the Cu precursor were subjected to ultrasonic treatment in an acetone solution (50 mL) for 4 h. The solvent was evaporated under vacuum at 80 °C for 12 h. The solid sample was dried and calcined in N_2 at 800 °C at a rate of 5 °C/min for 3 h. Finally, the dried sample was added to 0.5 M H_2SO_4 and maintained at 60 °C for 6 h to ensure complete leaching of Cu clusters and unreacted Cu ions. It was then thoroughly washed with deionized water until the pH was neutral, dried, and stored for later use.

2.3. Analytical methods

The performance of Cu-based single-atom catalysts were evaluated through the degradation reaction of BPA. A mixture of 0.125 g/L catalyst and 1.05 mM PDS was dispersed in 40 mL of BPA solution (10 mg/L), and continuously stirred in a beaker (unless otherwise specified). At fixed intervals, 1 mL of reaction solution was mixed with 0.5 mL of methanol to quench residual radicals. Filtrates were collected after filtration through 0.22 μm membrane for subsequent analysis. The quenching experiments were conducted by adding methanol, tert-butanol, furfuryl alcohol, oxalic acid, and EDTA-2Na during degradation. D_2O replaced deionized water as the solvent to validate the mechanism of $^1O_2$. For stability testing, the catalysts were washed with deionized water and ethanol after reaction, dried at 60 °C, and reused in subsequent cycles. Each experiment was repeated three times. Detailed characterization methods were provided in Text S2.

BPA concentrations were determined using high-performance liquid chromatography (HPLC, Waters Co.) equipped with an Agela Venusil C18 column (4.6 × 260 mm, 5 μm). HPLC analytical methods for various organic compounds were detailed in Table S1.

2.4. DFT calculation

We employed the Gaussian 16 and VASP software packages to perform DFT calculations, while completing geometric optimization and energy calculations under the detailed conditions described in Supplementary Text S3.

3. Results and discussion

3.1. Characterization

The N-HCMS@CuSA catalyst were fabricated following the procedure illustrated in Fig. 1a. As evidenced by the scanning electron microscopy (SEM, Fig. S1) and transmission electron microscopy (TEM, Fig. S2) images, both N-HCMS and N-HCMS@CuSA exhibited a distinct hollow spherical architecture. Notably, no aggregation of Cu nanoparticles was observed on the surface of catayst. To further scrutinize the atomic dispersion of the Cu species, high-angle annular dark-field scanning transmission electron microscopy (HAADF-STEM) was employed (Fig. 1b). The monodispersed bright spots corresponding to isolated Cu atoms were observed over the hollow mesoporous carbon matrix, confirming the atomic dispersion of Cu species in HCMS@CuSA. Furthermore, energy-dispersive X-ray spectroscopy (EDS) elemental mapping (Fig. 1c–e) confirmed the homogeneous distribution of C, N, and Cu throughout the catalyst, corroborating the absence of Cu nanoparticles. The X-ray diffraction (XRD) patterns of both the N-HCMS and N-HCMS@CuSA catalysts exhibited only a typical broad diffraction peak around 23°, which is attributed to the amorphous structure of the carbon layer (Fig. 1f) [39]. Notably, no characteristic peaks of crystalline Cu species (such as Cu nanoparticles or copper oxides) were detected in the N-HCMS@CuSA, excluding the existence of crystalline Cu species [40]. These results suggest that the Cu atoms are highly dispersed at the atomic level across the carbon matrix.

To elucidate the electronic structure and coordination environment of the Cu atoms in N-HCMS@CuSA, X-ray absorption near-edge structure (XANES) and extended X-ray absorption fine structure (EXAFS) measurements were examined. The XANES spectra demonstrated that the absorption edge position of N-HCMS@CuSA was located between the Cu_2O and CuO (Fig. S3a), indicating that the Cu atoms were coordinated in Cu(I) and Cu (II) forms. The Fourier-transform extended X-ray absorption fine structure (FT-EXAFS) spectrum of N-HCMS@CuSA (Fig. 1g) exhibited a prominent peak at 1.50 Å, which was ascribed to the first coordination shell of Cu—N bonding [41,42]. No characteristic signals of Cu—Cu and Cu—O were observed, indicating the absence of metallic crystalline Cu species. Furthermore, the corresponding WT-EXAFS analysis substantiated the lack of Cu—Cu and Cu—O bonds in N-HCMS@CuSA (Fig. 1i, Fig. S3b). Notably, the maximum k value at ~5.2 $Å^{-1}$ corresponded to Cu—N coordination; this feature aligns well with the profile of phthalocyanine copper (CuPc) [43]. The fitting results of EXAFS (Fig. 1h, Table S2) yielded indicated that Cu atom was coordinated with 4 N in the first shell with an average distance of 1.95 Å.

The N_2 adsorption-desorption isotherms and pore size distribution curves of N-HCMS and N-HCMS@CuSA were exhibited Fig. 2a. Both samples possessed Type IV isotherms with H4-type hysteresis loops at relative pressures ($P/P_o > 0.4$), indicative of rich mesoporous structures [44]. Meanwhile, the obvious upward curves under the relative pressures ($P/P_0 > 0.9$) for catalysts, ascribing to the cavity structure. The pore size distribution was calculated using the Barrett-Joyner-Halenda method based on the desorption branches [45]. Results showed that the average pore size of N-HCMS@CuSA (3.7 nm) was smaller than that of N-HCMS (9.7 nm). Owing to the unique porous shell structure, N-HCMS@CuSA(134.4 m^2g^{-1}) possessed higher specific surface area compared to N-HCMS(22.3 m^2g^{-1}) , which was beneficial to exposing active sites for activation (Table S3).

X-ray photoelectron spectroscopy (XPS) analysis was conducted to elucidate the chemical states and elemental composition of N-HCMS and N-HCMS@CuSA (Fig. 2b–d, Fig. S4). The distinct peak centered at 400.61 eV can be clearly found from the XPS spectrum(Fig. 2b), indicating the successful nitrogen doping [46,47]. Upon the introduction of Cu atoms, a new peak emerged near 398.4 eV in the N 1 s spectrum, which was assigned to the Cu—N interaction. Meanwhile, N 1 s XPS spectra of N-HCMS@CuSA catalysts showed a significant shift (1.24 eV) and a notable decrease in content of pyridine N in N-HCMS@CuSA as compared with that N-HCMS (Fig. 2c-d). This phenomenon implied that Cu single atoms were primarily coordinated with pyridinic N species to form a stable Cu—N_4 configuration. [48].

3.2. PDS activation performance of N-HCMS@CuSA

The catalytic performance of N-HCMS@CuSA was evaluated by the degradation of BPA with PDS activation. As shown in Fig. 3a, PDS alone only 19.6% removal of BPA. Adsorption indicated that approximately 21.3% of BPA was rapidly adsorbed onto the N-HCMS@CuSA surface. An experiment using the Cu^{2+}/PDS system was conducted; this yielded a removal efficiency of 22.4%, representing a marginal increase of only 3.4% compared to PDS alone, indicating that the Cu^{2+} potentially released from the catalyst played a negligible role in the degradation process. In the presence of PDS, the metal-free N-HCMS substrate reached a removal efficiency of 44.3%. In remarkably contrast with the pseudo-first-order rate constant (k_{obs}) of the Text S4 0.352 min^{-1} (Fig. 3b), which was significantly superior to that of the N-HCMS/PDS system (0.045 min^{-1}), representing a 7.5-fold improvement. To further

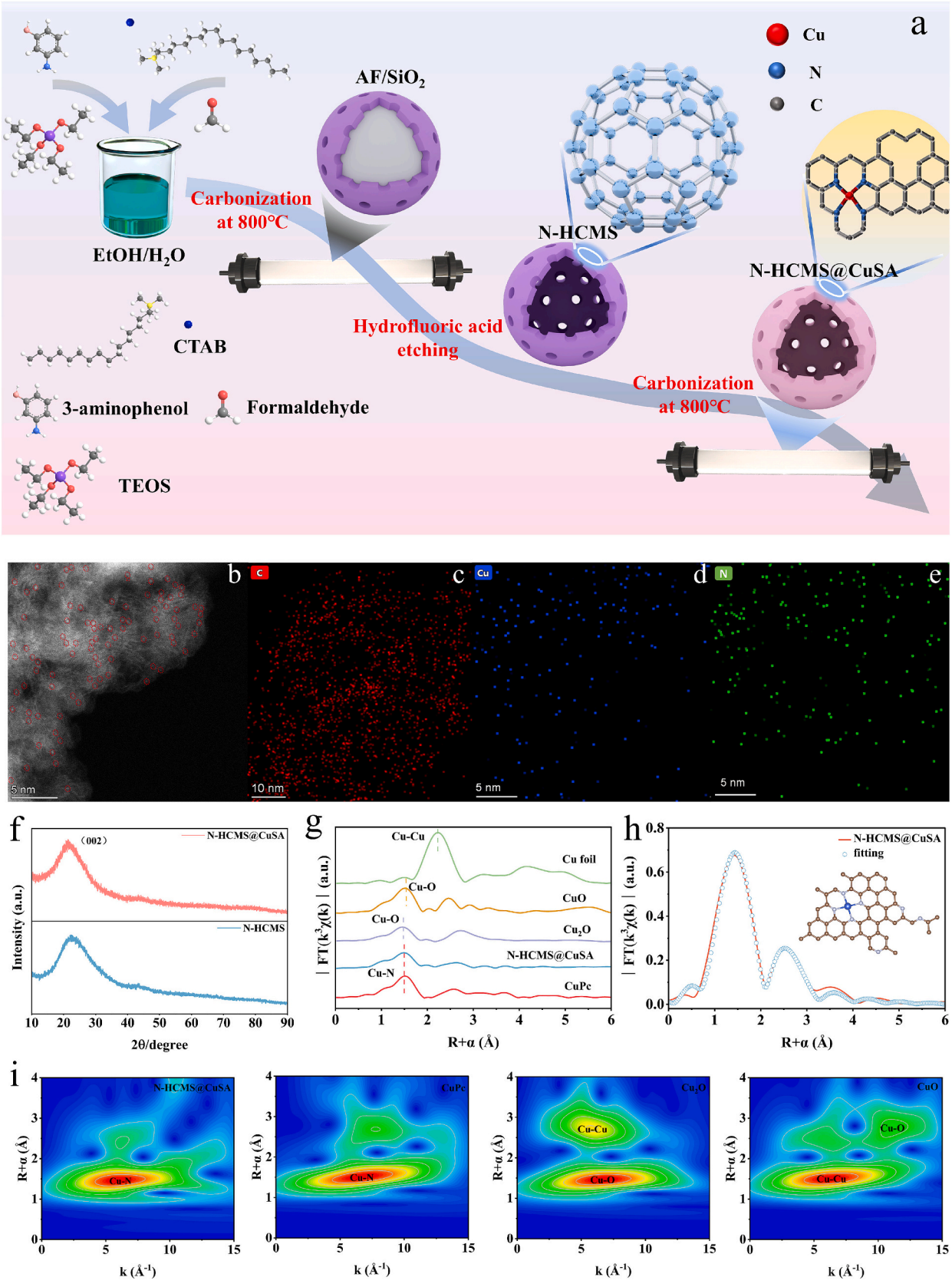

Fig. 1. (a) Synthesis pathway of N-HCMS@CuSA catalyst; (b) High-angle annular dark-field scanning transmission electron microscopy (HAADF-STEM) image of N-HCMS@CuSA and corresponding (c) C-site; (d) Cu-site; and (e) N-site EDS distribution maps; (f) X-ray diffraction pattern of N-HCMS@CuSA and N-HCMS; (g) FT-EXAFS spectrum of N-HCMS@CuSA; (h) R-space fitting curve of the EXAFS spectrum for N-HCMS@CuSA; (i) WT-EXAFS spectra of different samples.

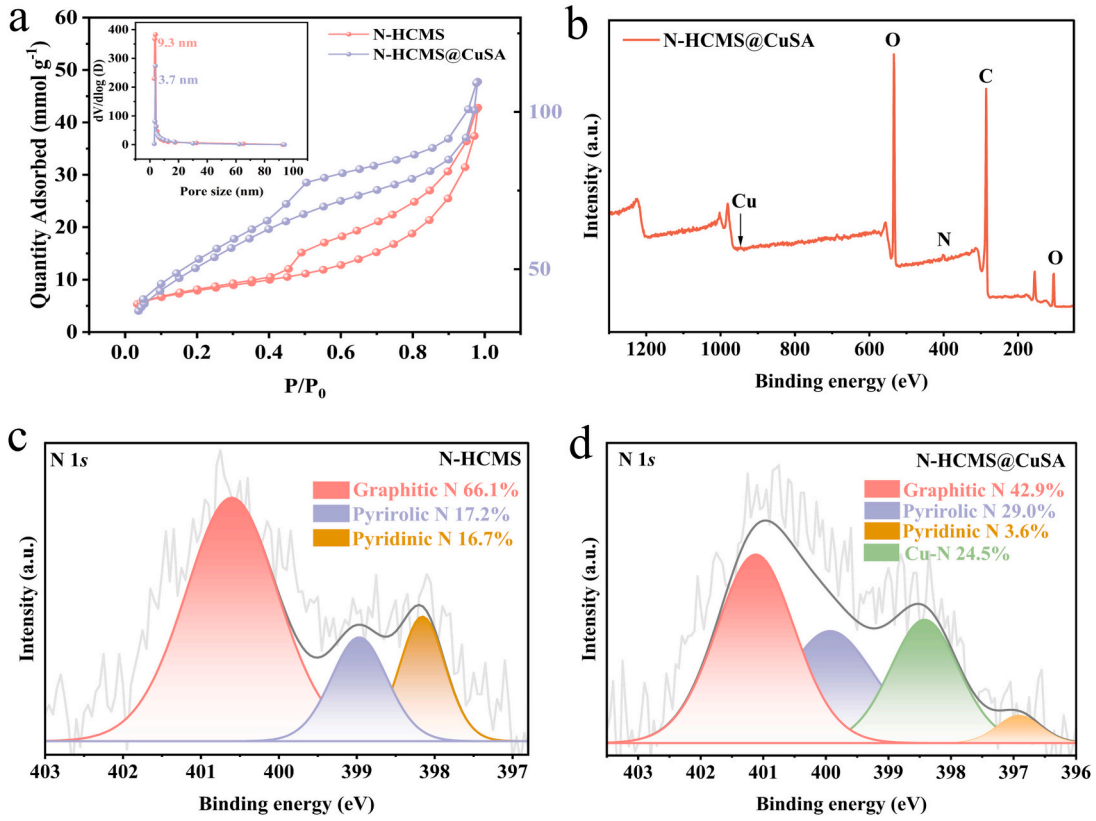

Fig. 2. (a) N_2 adsorption-desorption isotherms and pore size distribution curves of N-HCMS and N-HCMS@CuSA; (b) the full survey scan for N-HCMS@CuSA; (c) XPS N spectrum of N-HCMS; (d) XPS N spectrum of N-HCMS@CuSA.

quantify the intrinsic activity of the atomic Cu sites, the TOF was calculated based on the actual Cu loading of 0.16 wt% determined by ICP-OES. Remarkably, the N-HCMS@CuSA delivered a high TOF of 4.90 min^{-1} (details in Text S5). This confirmed that the atomically dispersed Cu—N_4 sites are maximally accessible and highly efficient for PDS activation. To highlight the specific activation superiority of our system toward PDS, a comparative degradation experiment was conducted using peroxymonosulfate (PMS) as an alternative oxidant. As illustrated in Fig. S5, the N-HCMS@CuSA/PMS system exhibited a significantly lower BPA degradation efficiency (only 56% within 12 min) compared to the complete removal achieved by the PDS system. Furthermore, optimization experiments indicated that even at a catalyst dosage of 5 mg and PDS dosage of 10 mg, the system achieved complete BPA degradation within 12 min (Fig.S6), demonstrating the catalyst's superior intrinsic activity and atom utilization efficiency. A comparison with state-of-the-art catalysts (Fig. 3c and Table S4) presented that N-HCMS@CuSA presented outstanding efficiency in activating PDS for BPA degradation. The results demonstrated the exceptionally high activity of N-HCMS@CuSA in the heterogeneous activation of PDS for BPA degradation. The TOC removal was further measured as an indicator of BPA mineralization. The N-HCMS@CuSA exhibited mineralization efficiency of 69.7% within 60 min (Fig. S7). Given that the degradation process was often sensitive to pH, the effect of solution pH was examined. The results showed that nearly complete degradation of BPA was achieved within 12 min over a wide pH span (3–9) (Fig. S8), demonstrating that N-HCMS@CuSA may be performed efficiently for the major role in the PDS activation process under neutral pH condition. The findings underscored the high efficiency of the N-HCMS@CuSA/PDS system across a broad pH spectrum. Regarding the structural stability, the leaching of Cu ions was found to be negligible. Specifically, Cu^{2+} leaching rates were limited to 0.16% and 0.19% under acidic and alkaline conditions, respectively, and dropped to 0.01% at pH 6 (Fig. S9). In addition, the BPA degradation was completed within 12 min in the buffered system of pH 6 (Fig. S10). The sustained high efficiency in the buffered environment confirms that the superior performance of N-HCMS@CuSA is derived from its intrinsic catalytic activity rather than pH acidification. In terms of reusability, the material maintained a degradation efficiency of 73.2% after five consecutive cycles (Fig. S11), demonstrating its ability to sustain catalytic performance during repeated operations. Furthermore, XRD analysis (Fig. S12) showed no discernible changes in the diffraction patterns compared to the fresh catalyst, corroborating its excellent structural integrity, demonstrating its ability to sustain degradation efficiency for repeated operation.

To evaluate the practical feasibility of the N-HCMS@CuSA/PDS system, BPA degradation experiments were conducted in real water matrices, including tap water and surface water (collected from Wuliangsuhai Lake). The detailed physicochemical parameters of these water samples including TOC and representative anions (e.g., Cl^-, SO_4^{2-}, HCO_3^-, and F^-) were summarized in Table S5. Remarkably, the system achieved complete removal within just 12 min in both water samples (Fig. S13). These results attested to acceptable adaptability of the N-HCMS@CuSA/PDS system, demonstrating its capability to maintain effective catalytic performance with complex aqueous matrices.

A continuous-flow setup was constructed to assess the practical potential of the N-HCMS@CuSA system using a catalyst-loaded polyurethane sponge as detailed in Text S6. The influent mixture of PDS and BPA was pumped upward at a flow rate of 2 mL min^{-1} through the reactor (Fig. 3d and Fig. S14). Continuous-flow experiments were conducted using a catalytic filter loaded with 110 mg of N-HCMS@CuSA over a 10-h reaction period. SEM analysis confirmed the dense fibrous morphology of the loaded sponge (Fig. S15). The system demonstrated superior performance and maintained a BPA degradation efficiency exceeding 94% throughout the process, which significantly outperformed control groups including N-HCMS-loaded PU/PDS, pristine

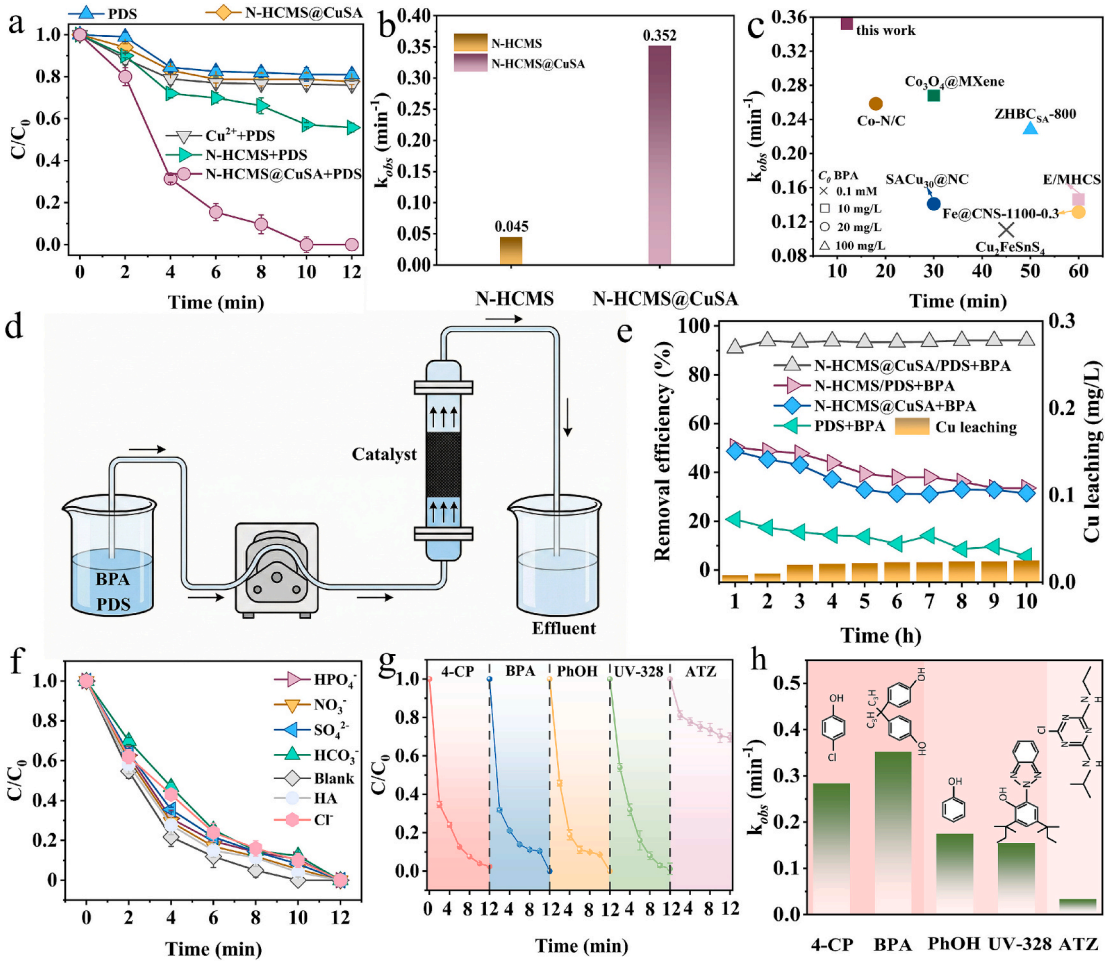

Fig. 3. (a) Degradation of BPA in different systems; (b) corresponding reaction kinetic constants; (c) comparison of BPA degradation efficiency in different persulfate systems; (d) Flow experimental apparatus; (e) continuous-flow performance of different systems for BPA removal; (f) effect of different anions on BPA degradation; (g) degradation efficiency of different pollutants in the N-HCMS@CuSA/PDS system; (h) corresponding k_{obs} values. (catalyst dosage = 0.125 g/L, $[PDS]_0$ = 0.25 g/L, $[BPA]_0$ = 10 mg/L, $[HPO_4^-]_0 = [NO_3^-]_0 = [SO_4^{2-}]_0 = [HCO_3^-]_0$ = 10 mM, $[4\text{-CP}]_0 = [PhOH]_0 = [UV\text{-}328]_0 = [ATZ]_0$ = 10 mg/L, T = 25 °C, pH = 6).

PU/PDS, and N-HCMS@CuSA-loaded PU alone (Fig. 3e). Furthermore, the catalyst exhibited excellent stability with a maximum copper leaching concentration of only 0.02 mg/L detected during long-term continuous operation. Collectively, these results confirm the high efficacy and structural integrity of the N-HCMS@CuSA-loaded PU/PDS system against complex actual wastewater matrices, making it exceptionally suitable as a robust pre-treatment strategy to mitigate organic fouling in downstream membrane processes. As depicted in Fig. 3f, the degradation performance remained largely unaffected, achieving 100% BPA removal even in the presence of various interfering anions including Cl^-, HPO_4^-, NO_3^-, SO_4^{2-}, and HCO_3^-. Furthermore, the humic acid (HA) had a negligible impact on the efficiency. This exceptional anti-interference capability highlights the good resistance of the N-HCMS@CuSA/PDS system toward target pollutants. The N-HCMS@CuSA system demonstrates scalability potential for engineering applications. Specifically, the macroscopic immobilization of the powder catalyst within the PU sponge framework effectively addresses the ubiquitous separation challenges associated with nanomaterials, precluding the need for energy-intensive post-treatment steps. Moreover, the demonstrated stability under continuous-flow conditions underscores the high compatibility of this structured catalyst with industrial fixed-bed column configurations. In addition, driven by the overwhelmingly dominant DET mechanism, the system exhibits resistance to background interference from ubiquitous anions and organic matter (TOC) present in real water matrices. This specific feature minimizes the futile consumption of the oxidant and maintains steady performance in complex practical environments, highlighting its tremendous potential as a reliable pre-treatment strategy for advanced desalination and wastewater reclamation.

The N-HCMS@CuSA catalyst exhibited exceptional versatility in degrading various persistent organic pollutants via PDS activation. As presented in Fig. 3g and h, removal efficiencies exceeding 98.8% were achieved within 12 min for 4-chlorophenol (4-CP), BPA, phenol (PhOH), and 2-(2H-benzotriazol-2-yl)-4,6-di-tert-pentylphenol (UV-328). In contrast, atrazine (ATZ) demonstrated limited degradation (kobs = 0.033 min^{-1}), with a removal efficiency of only 31.5%. It indicated that the N-HCMS@CuSA/PDS system possessed specific oxidative selectivity toward electron-rich organic substrates.

The cyclic voltammetry(CV) measurements were conducted to determine the redox potentials of the pollutants [49]. The half-wave potential ($\varphi_{1/2}$) served as a key indicator of the oxidizability of these compounds (Fig. S16). Specifically, for BPA, the anodic peak (1a) located at 0.622 V (Fig. 4a) corresponded to a calculated $\varphi_{1/2}$ value of 0.476 eV, based on Eq. S2 (Text S7). Fig. 4b summarized the $\varphi_{1/2}$ values, which followed the increasing order: BPA < 4-CP < PhOH < UV-328 < ATZ. Subsequently, a correlation was established between k_{obs} and $\varphi_{1/2}$ (Fig. 4c). A strong linear correlation (R^2 = 0.942) was observed for the four oxidized pollutants (BPA, 4-CP, PhOH, UV-328), whereas ATZ showed a significantly higher $\varphi_{1/2}$ value. Generally, contaminants with low $\varphi_{1/2}$ values demonstrated high oxidation rates, while ATZ with its

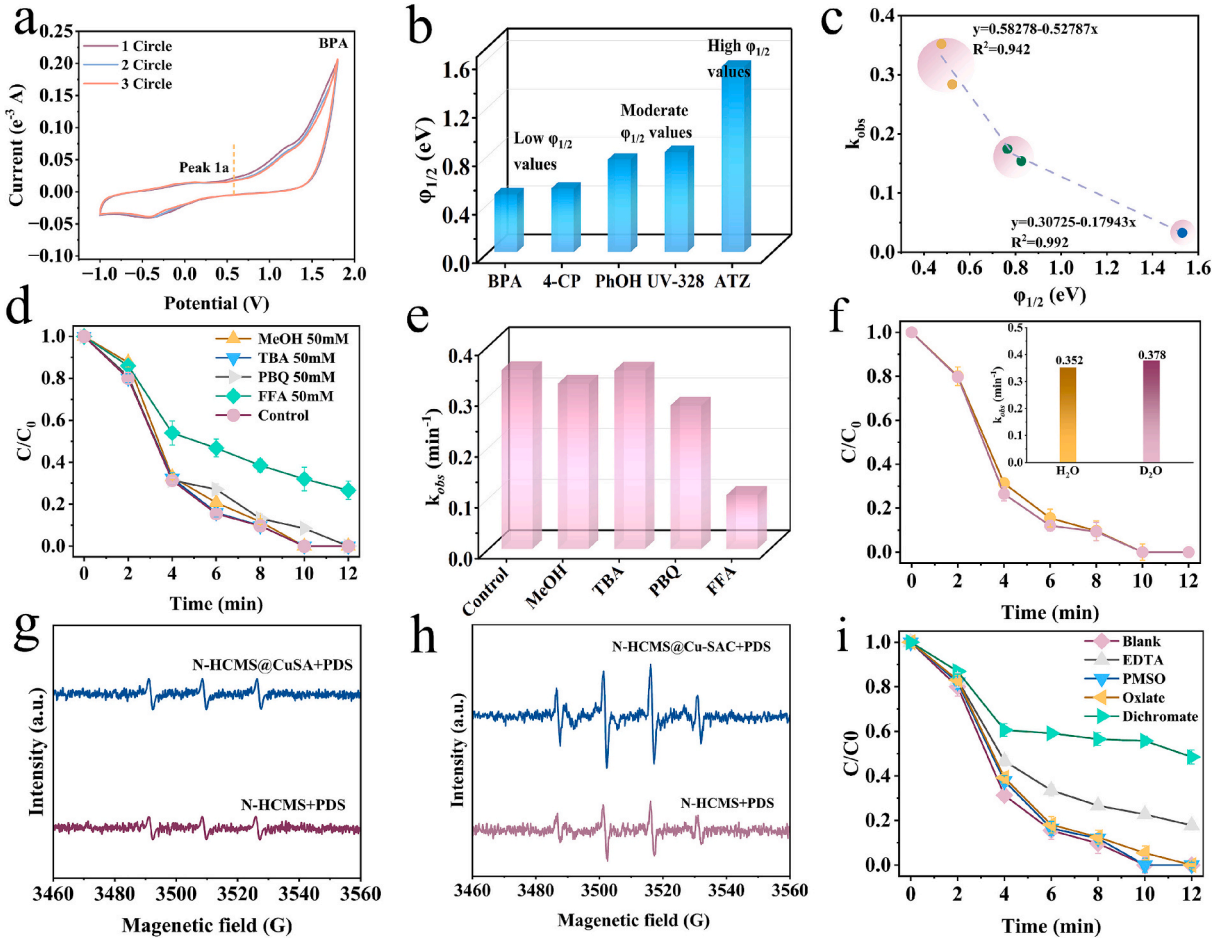

Fig. 4. (a) CV curve of BPA; (b) $\varphi_{1/2}$ values of different pollutants; (c) correlation between $\varphi_{1/2}$ values and k_{obs} of different pollutants; (d) effect of quenchers on BPA degradation in the N-HCMS@CuSA/PDS system; (e) and corresponding reaction rate constants; (f) effect of deuterated water on BPA degradation in the N-HCMS@CuSA/PDS system; EPR spectra of (g) $^1O_2$ and (h) sulfate radical ($SO_4^{\bullet-}$/·OH) in different N-HCMS@CuSA/PDS/BPA systems; (i) effects of PMSO, oxalate, EDTA, and dichromate on BPA degradation kinetics. (catalyst dosage = 0.125 g/L, $[PDS]_0$ = 0.25 g/L, $[BPA]_0$ = 10 mg/L , $[EDTA]_0$ = $[Oxlate]_0$ = 10 mM , $[PMSO]_0$ = 0.2 mM, $[Dirchromate]_0$ = 20 Mm, T = 25 °C, pH = 6).

high potential showed suppressed kinetics. The results implied that the degradation efficiency was intrinsically linked to the redox potential of the contaminant.

3.3. Mechanism of activated PDS for BPA degradation

3.3.1. Identification of active species

The mechanism of BPA removal was investigated using quenching studies to identify the reactive species. Methanol (MeOH) and tert-butanol (TBA) were employed as scavengers for hydroxyl radicals (·OH) and sulfate radicals ($SO_4^{\bullet-}$), respectively [50]. As depicted in Fig. 4d, the addition of MeOH or TBA to the reaction system exerted a negligible inhibitory effect on BPA degradation. Quantitatively, the pseudo-first-order rate constants in the presence of MeOH (0.325 min^{-1}) and TBA (0.351 min^{-1}) were virtually identical to that of the blank control (0.352 min^{-1}) (Fig. 4e). It implied that ·OH and $SO_4^{\bullet-}$ were not the primary active species driving the degradation process. Additionally, EPR analyses confirmed the generation of reactive radicals of ·OH and $SO_4^{\bullet-}$ (Fig. 4g). These findings demonstrate that while radical-mediated oxidation universally occurs, its contribution varies markly pollutants. P-benzoquinone (PBQ) was employed to scavenge superoxide radicals ($O_2^{\bullet-}$), the inhibitory effect was minimal, indicating that the contribution of $O_2^{\bullet-}$ to BPA degradation is negligible. In contrast, the addition of furfuryl alcohol (FFA), a specific scavenger for singlet oxygen ($^1O_2$) [51], significantly suppressed the degradation process. While this inhibition is traditionally ascribed to ROS quenching, it can be more plausibly explained by a substrate competition mechanism [52]. As an electron-rich molecule, FFA competitively coordinates with the catalyst's active sites, effectively blocking BPA access and consequently retarding the overall degradation kinetics [53]. To further validate this hypothesis, L-histidine was employed as another highly specific $^1O_2$ scavenger. Distinct from FFA, the presence of L-histidine exhibited little to no inhibition of BPA degradation (Fig. S17). This outcome confirms that the FFA-induced inhibition is primarily attributed to competitive oxidation rather than $^1O_2$ consumption. Given the potential selectivity limitations of chemical scavengers, EPR spectra were obtained to investigate the role of $^1O_2$. Fig. 4g displayed only a faint TEMP-$^1O_2$ peak in the N-HCMS@CuSA/PDS system, implying that the involvement of $^1O_2$ was excluded. Degradation experiments were performed using heavy water(D_2O). Despite the fact that the lifetime of $^1O_2$ in D_2O was longer than that in H_2O [54] , the BPA degradation rate and reaction rate constant in D_2O was nearly identical to that in H_2O as presented in Fig. 4f. The above results ruled out singlet oxygen as the primary active species. Consequently, other nonradical mechanisms were present in the N-HCMS@CuSA/PDS system.

3.3.2. Direct electron transfer pathway

The previous report has documented that certain Cu-based single-atom catalysts activate PDS to generate high-valent Cu species via a dominant mechanism [55]. Typically, this process involved the binding

of PDS to Cu(II) sites to yield Cu(III)-O complexes capable of efficiently degrading organic contaminants. To verify whether such Cu(III) species function as the active oxidants in the N-HCMS@CuSA/PDS system, sodium oxalate and methyl phenyl sulfoxide (PMSO) were employed as specific probes. Sodium oxalate was known to undergo rapid redox reactions with Cu(III), while PMSO serves as an indicator by impeding Cu (III) formation through its oxidation to $PMSO_2$ via an oxygen atom transfer mechanism [56,57]. As displayed in Fig. 4i, the introduction of either sodium oxalate or PMSO into the reaction system resulted in negligible inhibition of BPA removal. This result excluded the generation of Cu(III) during the catalytic process. Besides, the degradation rate of PE dramatically declined in N-HCMS@CuSA /PDS with the addition of EDTA to poison the metal site. This result indicated the critical role of Cu—N_4 sites in PDS activation These results strongly suggested the existence of a non-radical pathway involving the Cu—N_4 active site in the N-HCMS@CuSA/PDS system.

The DET is increasingly recognized as a pivotal mechanism for organic degradation in advanced oxidation processes [58]. To preliminarily explore the specific degradation pathway of BPA within the N-HCMS@CuSA/PDS system, dichromate was introduced to inhibit direct electron transfer. Functioning as a potent electron scavenger, dichromate can competitively intercept the interfacial electron transform from the substrate [59]. Consequently, the degradation rate of BPA was markedly suppressed upon the addition of dichromate. Therefore, subsequent electrochemical analysis and galvanic oxidation system (GOS) analyses were conducted. [60].

Electrochemical analysis was used to identify the DET regime. As illustrated in the linear sweep voltammetry (LSV) profiles in Fig. 5a, the current density of the N-HCMS@CuSA electrode revealed a pronounced current response upon the introduction of PDS, signifying electron transfer from the catalyst to PDS. The subsequent addition of BPA displayed distinct current response, which substantiated the existence of the continuous electron transfer pathway. Furthermore, the chronoamperometric response shown in Fig. 5b displayed distinct current steps following the sequential injection of PDS (0.5 mM) and BPA (10 mg/L). Collectively, these results provided compelling evidence of electron transform among N-HCMS@CuSA, PDS, and BPA. In contrast, the N-HCMS system exhibited no detectable current response upon PDS addition, which attributed to the high impedance of the metal-free support. Further insight is provided by the electrochemical impedance spectroscopy Nyquist plots in Fig. 5c, where the semicircular region corresponds to the charge transfer resistance, while the linear portion is associated with mass transfer resistance [61]. The smaller semicircular radius observed for N-HCMS@CuSA reflects a reduced resistance to charge transfer, which supported the finding of the highest reaction rate in the PDS/BPA system. As shown in Fig. 5d, the CV analysis showed that N-HCMS@CuSA generated higher current density than the N-HCMS support, proving that Cu single atoms are essential for activating PDS and superior activity. [62,63].

A galvanic oxidation system (GOS) was constructed to probe the electron-transfer behavior between BPA and the N-HCMS@CuSA/PDS system (Text S8) [64].In this setup, PDS and BPA were isolated in two cells with N-HCMS@CuSA-modified graphite flakes as electrodes. The chambers were connected by a salt bridge and a galvanometer to monitor [65] current. Adding PDS and BPA caused current fluctuations, peaking at 56 μA then dropping to 26.7 μA in 12 min. This decay is due to reaction kinetics and mass transfer limits, shifting from kinetic to diffusion control. Similar currents with unmodified graphite sheets show graphite's intrinsic ability to activate PDS via electron transfer. Thus, direct electron transfer is the primary mechanism in the N-HCMS@CuSA/PDS system.

In summary, the experimental results confirm the dominant role of the DET pathway in the N-HCMS@CuSA/PDS system. The advantages of DET pathway become particularly evident when contrasted with other reported catalytic systems. Previous studies have demonstrated that Cu-based single-atom catalysts typically activate PDS via the generation of ROS, such as $^1O_2$, or the formation of high-valent copper intermediates (e.g., Cu(III)) [66,67]. However, $^1O_2$ and Cu(III) species can still suffer from futile consumption by ubiquitous NOM or background inorganic ions in complex aquatic environments, leading to reduced utilization efficiency of the oxidant [68]. In contrast, the highly confined Cu—N_4 active sites in N-HCMS@CuSA exclusively trigger a DET pathway [69].

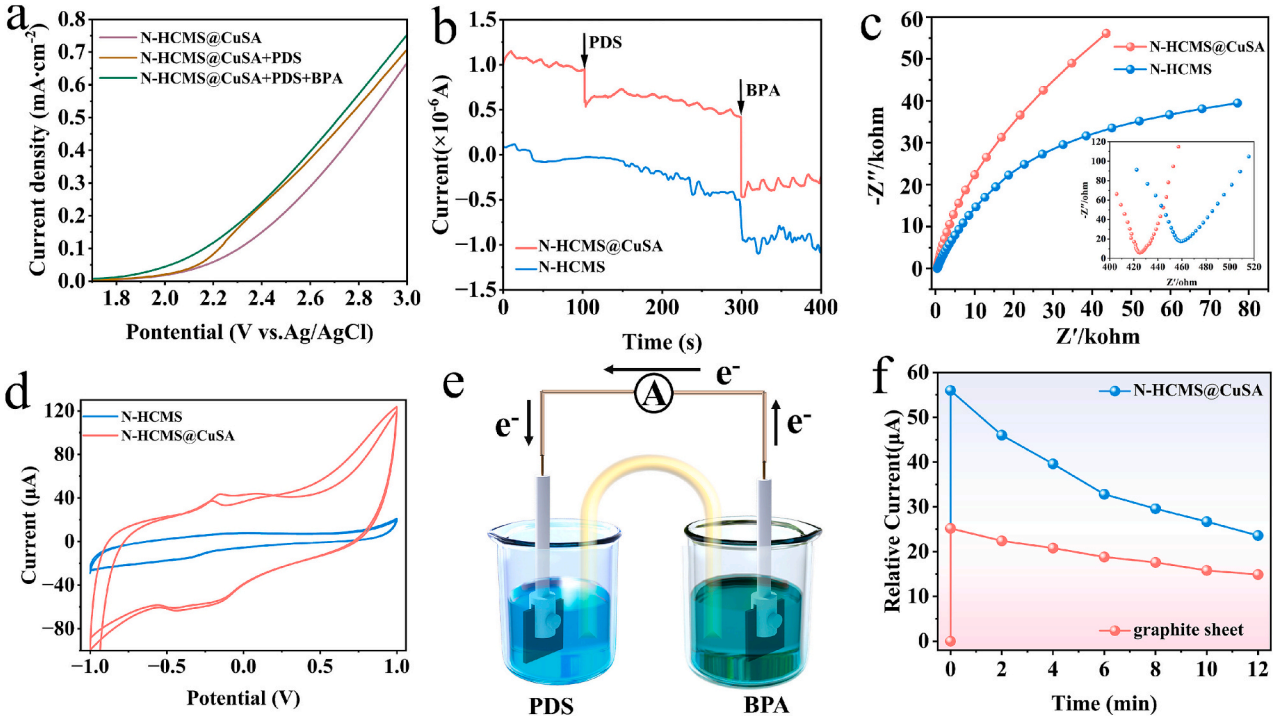

Fig. 5. (a) LSV curve of N-HCMS@CuSA; (b) i-t curve of N-HCMS and N-HCMS@CuSA; (c) Nyquist plot of N-HCMS and N-HCMS@CuSA; (d) CV curve of N-HCMS and N-HCMS@CuSA; (e) design schematic of the GOS device; (f) current flow from the PDS electrolyzer to the contaminant in the GOS.

By serving as an efficient electron bridge, the Cu-N_4 sites facilitate the direct transfer of electrons from the electron-donating BPA to the electron-accepting PDS [70]. Consequently, the dominance of this non-radical bridging pathway prevents the consumption of PDS by background constituents, endowing the system with remarkable anti-interference capabilities in real wastewater matrices [71].

3.4. DFT calculations

DFT calculations were performed to elucidate the intrinsic mechanism of PDS activation by N-HCMS@CuSA. It is well established that the adsorption configuration of reactants plays a pivotal role in the reaction kinetics [72]. Fig. 6a and b displayed the optimized geometric structures of HCMS and N-HCMS@CuSA, respectively. To probe the interaction mechanism, the adsorption and activation behaviors of PDS on both substrates were simulated. As depicted in Fig. 6c and d, the calculated adsorption energy of PDS on N-HCMS@CuSA is −2.0 eV, which is significantly more negative than that on N-HCMS (−0.39 eV). This energy difference indicates an affinity between the PDS molecule and the N-HCMS@CuSA surface. Interaction with the catalyst causes the PDS molecule to distort, stretching its O—O bond from 1.493 Å to 1.502 Å (Fig. S18), while the proximal S—O bond is stretched to 1.648 Å compared to 1.482 Å at the N-HCMS site. This simultaneous elongation confirms that the PDS molecule is chemically activated. Crucially, the O—O bond remains intact rather than undergoing spontaneous cleavage, pointing to the formation of a metastable chemisorbed intermediate. (details in Text S9). Furthermore, role of interfacial interactions on electron redistribution was investigated via Bader charge analysis. Fig. 6e demonstrated that the N-HCMS interface exhibits only negligible charge redistribution, with a minimal charge transfer of 0.016 |e| from the substrate to PDS. In contrast, the charge density difference analysis visualized in Fig. 6f illustrated substantial charge accumulation upon PDS adsorption on N-HCMS@CuSA. A significant Bader charge transfer of 1.352 |e| was calculated from the Cu—N_4 sites to the PDS molecule, demonstrating highly efficient interfacial electron on catalyst d. These differential charge results indicated that the incorporation of Cu—N_4 motifs effectively modulates the spin density and electronic distribution [73]. Furthermore, Fig. 6g illustrated the Gibbs free energy profiles of the reaction pathway. The negative adsorption energy of all the samples indicated that PDS activation was thermodynamically favorable. Mechanistically, the Cu—N_4 active center functions as an electron mediator; it extracted an electron from the pollutant and concurrently shuttles electrons to the PDS. This electron injection triggers the cleavage of the O—O bond, yielding two SO_4^{2-} anions. Ultimately, the generated SO_4^{2-} species desorb from the catalyst surface to regenerate the active site.

For the N-HCMS substrate, the activation energy barrier for PDS was calculated to be 3.5 eV, accompanied by a highly positive overall reaction free energy of +5.02 eV. These distinctively high energy values indicate that the N-HCMS support is highly inert toward PDS, which makes the cleavage of the O—O bond thermodynamically and kinetically unfavorable to occur [74]. In addition, the N-HCMS@CuSA catalyst exhibited a drastically reduced activation barrier of 1.70 eV and a much lower reaction free energy of +0.83 eV compared to N-HCMS. This

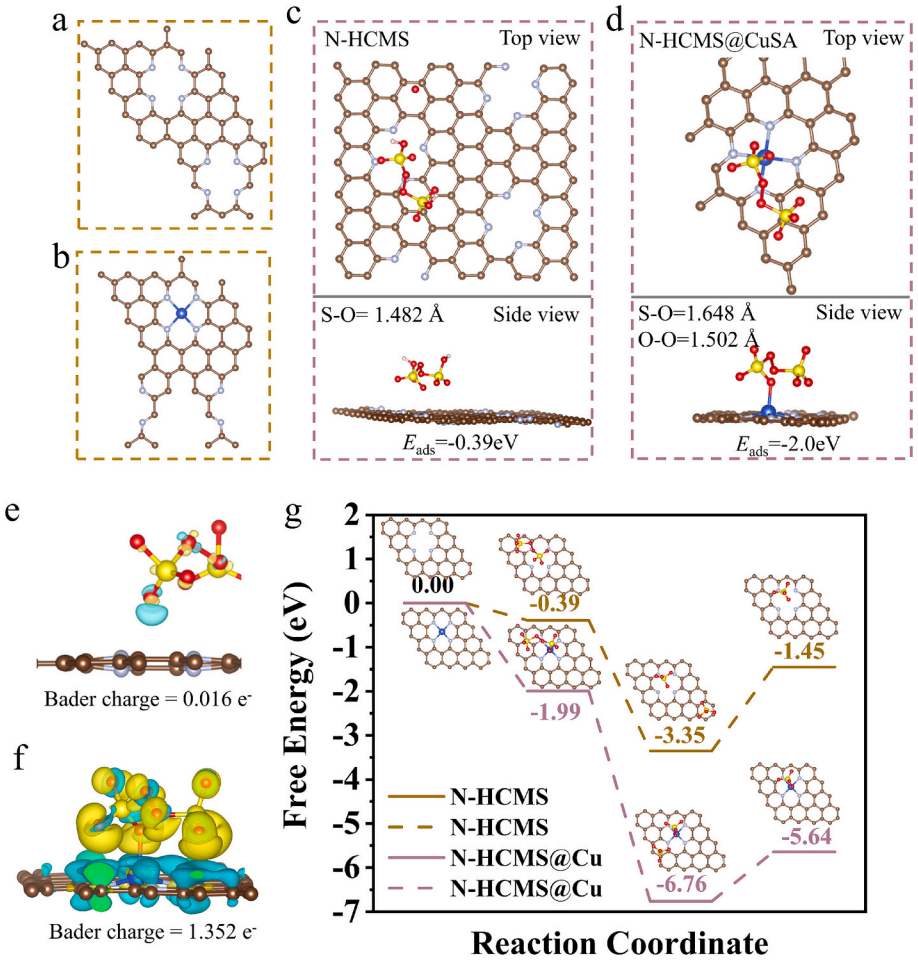

Fig. 6. (a) DFT-calculated structural models of N-HCMS and (b) N-HCMS@CuSA; adsorption structures and energies of PDS on (c) N-HCMS and (d) N-HCMS@CuSA; charge density difference maps of PDS on (e) N-HCMS and (f) N-HCMS@CuSA; (g) Energy response plot at the Cu—N_4 site.

trend aligns perfectly with the differential charge density analysis, confirming that Cu single atoms function as efficient electron donors to activate PDS, thereby facilitating the electron transfer during organic degradation. Consequently, the strong agreement between the theoretical DFT calculations and the experimental ROS identification, validly confirming the process mediated by the Cu single-atom sites.

3.5. Degradation pathways and toxicity analysis of degradation intermediate

To elucidate the degradation mechanisms of BPA within the N-HCMS@CuSA/PDS system, the reaction intermediates were detected and characterized via LC-MS/MS [75]. The possible degradation pathways were proposed in Fig. 7a. In Pathway I, the process involved an electron transfer-induced attack on the benzene ring, leading to ring-opening and the formation of P9. Crucially; In Pathway II, the generation of the hydroxylated product P8 is mainly mediated by the non-radical DET process rather than direct radical oxidation. Furthermore, in Pathway III, the oxidative transformation of BPA is proposed to be induced by the DET mechanism.

This interaction promoted β-cleavage (C—C bond scission) to yield P1 or P2 [76]. Subsequently, P1 was hydroxylated to evolve into P3, P4, or P5. Following this, P3 undergoes further oxidation via dealkylation and hydroxylation to convert into P4 and P7, a sequence consistent with literature precedents. Corroborated by TOC analysis, these intermediates were ultimately mineralized into CO_2 and H_2O. Notably, the mass spectra displayed in Fig. S19 exhibited the high peak areas for P1 and P2, thereby suggesting Pathway III as the predominant degradation route in the N-HCMS@CuSA/PDS system.

Given the concern that degradation processes may inadvertently yield more toxic intermediates, the Ecological Structure-Activity Relationship (ECOSAR) model was employed to rigorously assess the toxicity evolution during BPA degradation by the N-HCMS@CuSA/PDS system [77]. The predicted ecotoxicity values for BPA and its transformation products were summarized in Table S6. According to the Globally Harmonized System (GHS) of Classification and Labelling of Chemicals, acute aquatic toxicity can be classified by threshold values: very toxic (<1 mg/L), toxic (1–10 mg/L), harmful (10–100 mg/L), and not classified/non-toxic (>100 mg/L). The parent BPA imposed significant acute and chronic risks to aquatic ecosystems, specifically exhibiting toxicity values of 6.27/0.733 mg/L for fish, 4.15/0.617 mg/L for *Daphnia magna*, and 5.78/0.617 mg/L for green algae [78]. However, the toxicity profiles manifested in Fig. 7b and c demonstrated that nearly all degradation intermediates possess substantially lower acute and chronic toxicity toward three trophic levels. P8 retained toxicity levels comparable to those of the parent BPA. However, as evidenced by its low relative abundance, P8 served solely as a transient intermediate formed via the minor Pathway II. It would undergo rapid subsequent ring-opening and decomposition without significant accumulation, thereby posing negligible secondary ecological risks. In conclusion, by virtue of

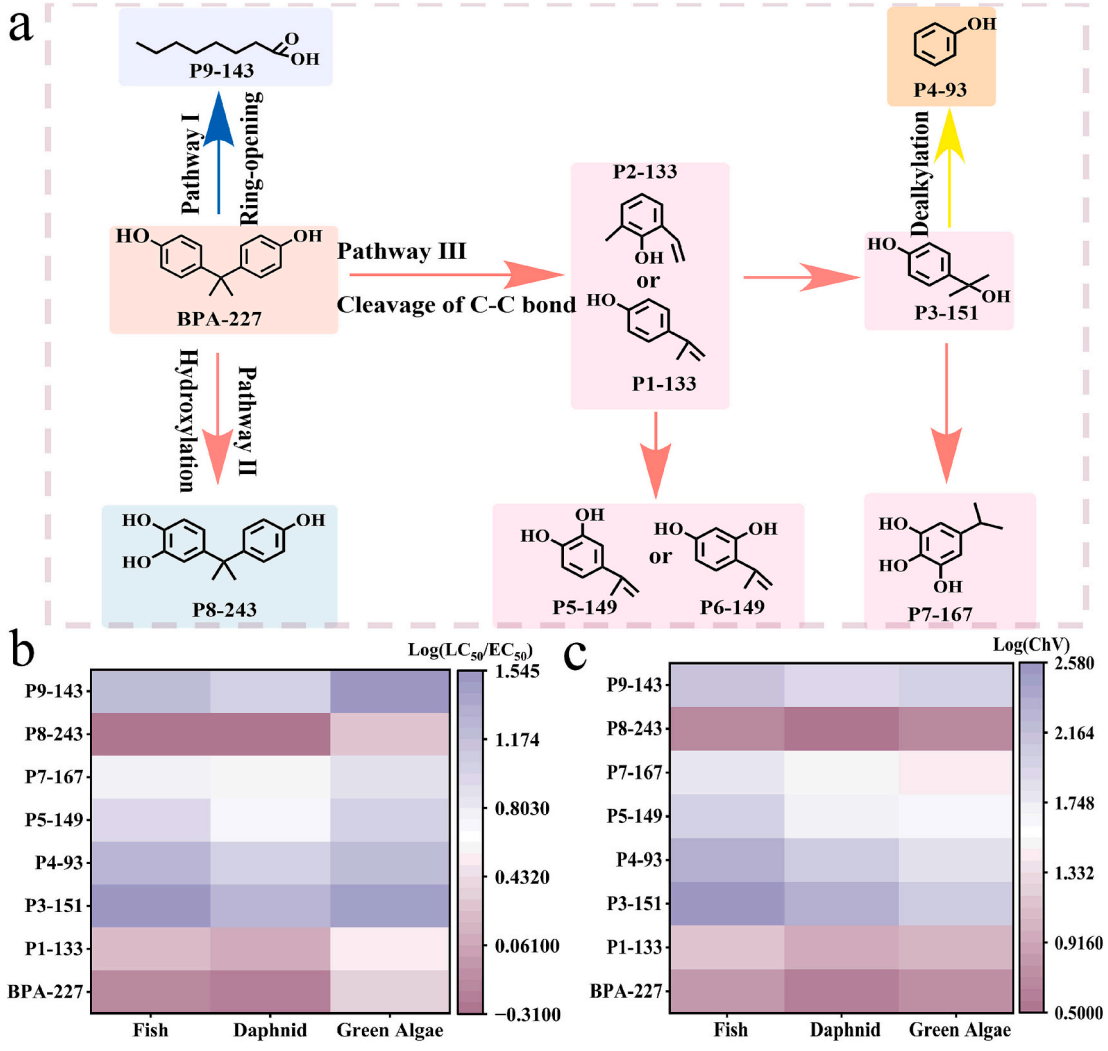

Fig. 7. (a) Degradation pathways of BPA in the N-HCMS@CuSA/PDS system, (b) acute toxicity of BPA and seven intermediate reaction products, (c) chronic toxicity.

exceptional catalytic activity, structural stability, and favorable detoxification trends, N-HCMS@CuSA stands out as a promising candidate for the remediation of emerging organic pollutants.

4. Conclusion

In summary, a hollow mesoporous carbon-based Cu single-atom catalyst (N-HCMS@CuSA) was developed for the highly efficient purification of organic wastewater via PDS activation. The catalyst achieves a turnover frequency (TOF) of 4.90 min^{-1}, which significantly surpasses that of state-of-the-art Cu-based catalysts. This study identified a DET regime. We established a robust positive correlation between the k_{obs} and the $\varphi_{1/2}$ of various pollutants. This thermodynamic relationship confirmed that the degradation is governed by electron transfer efficiency, where compounds with low $\varphi_{1/2}$ were preferentially degraded. Crucially, based on electrochemical analysis and DFT calculations, it was established the degradation of contaminants in the N-HCMS@CuSA/PDS system was driven by DET. DFT calculations further elucidated that the intrinsic Cu—N_4 sites modulate the electronic structure to induce strong Cu—O covalent interactions, effectively elongating the O—O bond of adsorbed PDS rapid interfacial oxidation. Benefiting from the robust carbon architecture and the efficient DET pathway, N-HCMS@CuSA exhibited exceptional resistance to environmental interference and sustained high stability in a 10 h continuous flow operation. Moreover, toxicity assessments confirmed that the degradation pathway yields low toxicity intermediates, ensuring biological safety. Consequently, this work not only provides a mechanistic basis for designing stable single-atom catalysts but also highlights the immense potential of the N-HCMS@CuSA/PDS system as a robust pretreatment technology to mitigate organic fouling and protect membranes in advanced water reclamation facilities.

CRediT authorship contribution statement

Xueyang Fan: Writing – review & editing, Writing – original draft, Methodology, Investigation, Conceptualization. **Yuxuan Zhang:** Methodology, Investigation, Conceptualization. **Zhenjun Tian:** Supervision, Conceptualization. **Shengwang Gao:** Writing – review & editing, Writing – original draft, Investigation. **Caili Du:** Investigation, Conceptualization. **Yangwei Bai:** Writing – original draft. **Lieyu Zhang:** Writing – review & editing, Project administration, Funding acquisition.

Declaration of competing interest

The authors declare that they have no known competing financial interests or personal relationships that could have appeared to influence the work reported in this paper.

Acknowledgments

This work was supported by the National Key Research and Development Program (2022YFD1601000).

Appendix A. Supplementary data

Supplementary data to this article can be found online at https://doi.org/10.1016/j.desal.2026.120500.

Data availability

Data will be made available on request.

References

[1] S.Y. Zhang, R.P. Wang, K. Wang, M. Wang, Z.X. He, H.L. Chen, S.H. Ho, Aeration-free in situ Fenton-like reaction: specific adsorption and activation of oxygen on heterophase oxygen vacancies, Environ. Sci. Technol. 58 (2024) 1921–1933, https://doi.org/10.1021/acs.est.3c08579.
[2] W.W. Ben, B. Zhu, X.J. Yuan, Y. Zhang, M. Yang, Z.M. Qiang, Occurrence, removal and risk of organic micropollutants in wastewater treatment plants across China: comparison of wastewater treatment processes, Water Res. 130 (2018) 38–46, https://doi.org/10.1016/j.watres.2017.11.057.
[3] M. Qasim, M. Badrelzaman, N.N. Darwish, N.A. Darwish, N. Hilal, Reverse osmosis desalination: a state-of-the-art review, Desalination 459 (2019) 59–104, https://doi.org/10.1016/j.desal.2019.02.008.
[4] W. Ma, R. Han, L. Zhu, W. Zhang, H. Zhang, L. Jiang, L. Chen, Peroxymonosulfate enhanced Fe(III) coagulation coupled with membrane distillation for ammonia recovery: membrane fouling control process and mechanism, Desalination 565 (2023) 116859, https://doi.org/10.1016/j.desal.2023.116859.
[5] Q. Wu, Z. Yang, Z. Wang, W. Wang, Oxygen doping of cobalt-single-atom coordination enhances peroxymonosulfate activation and high-valent cobalt–oxo species formation, Proc. Natl. Acad. Sci. USA 120 (2023) e2219923120, https://doi.org/10.1073/pnas.2219923120.
[6] Z. Wu, Z. Xiong, B. Huang, G. Yao, S. Zhan, B. Lai, Long-range interactions driving neighboring Fe–N_4 sites in Fenton-like reactions for sustainable water decontamination, Nat. Commun. 15 (2024) 7775, https://doi.org/10.1038/s41467-024-52074-2.
[7] J. Yu, Z. Gong, S. Wang, H. Zhong, Y. Tao, Y. Hou, Q. Fu, H. Yang, J. Li, J. Wang, Z. Hao, G. Ouyang, Two major deactivation mechanisms in carbon-based advanced oxidation processes (AOPs) dominated by electron-transfer pathway (ETP), Appl. Catal. B Environ. Energy 364 (2025), https://doi.org/10.1016/j.apcatb.2024.124850.
[8] Z. Weng, Y. Lin, S. Guo, X. Zhang, Q. Guo, Y. Luo, X. Ou, J. Ma, Y. Zhou, J. Jiang, B. Han, Site engineering of covalent organic frameworks for regulating Peroxymonosulfate activation to generate singlet oxygen with 100% selectivity, Angew. Chem. Int. Ed. 62 (2023), https://doi.org/10.1002/anie.202310934.
[9] J. Pei, J. Liu, K. Fu, Y. Fu, K. Yin, S. Luo, D. Yu, M. Xing, J. Luo, Non-metallic iodine single-atom catalysts with optimized electronic structures for efficient Fenton-like reactions, Nat. Commun. 16 (2025) 800, https://doi.org/10.1038/s41467-025-56246-6.
[10] B. Chen, M. Zhang, L. Wang, L. Li, Q. Han, X. Liu, M. Wang, B. Liu, Y. Jiang, Z. Wang, Enhanced organic pollutant degradation in a two-dimensional Fe-doped crystalline carbon nitride membrane with near 100% singlet oxygen generation through the Fe-O-N configuration, Appl. Catal. B Environ. Energy 363 (2025), https://doi.org/10.1016/j.apcatb.2024.124827.
[11] Z. Guo, W. Wei, Y. Li, X. Niu, F. Hou, J. Li, X. Zhang, X. Zhang, A. Wei, Cu single atoms anchored on hydrangea-like carbon nitride for facilitating photo-Fenton: role of cu^{2+}/Cu^{+} cycle, Sep. Purif. Technol. 344 (2024) 127290, https://doi.org/10.1016/j.seppur.2024.127290.
[12] W. Ren, C. Cheng, P. Shao, X. Luo, H. Zhang, S. Wang, X. Duan, Origins of Electron-transfer regime in persulfate-based nonradical oxidation processes, Environ. Sci. Technol. 56 (2022) 78–97, https://doi.org/10.1021/acs.est.1c05374.
[13] D. Li, S. Zhang, S. Li, J. Tang, T. Hua, F. Li, Mechanism of the application of single-atom catalyst-activated PMS/PDS to the degradation of organic pollutants in water environment: a review, J. Clean. Prod. 397 (2023) 136468, https://doi.org/10.1016/j.jclepro.2023.136468.
[14] Y. Huang, K. Chen, S. Wang, S. Zhao, L. Yu, B. Huang, R. Jin, Synergizing electron transfer with singlet oxygen to expedite refractory contaminant mineralization in peroxymonosulfate based heterogeneous oxidation system, Appl. Catal. B Environ. Energy 341 (2024), https://doi.org/10.1016/j.apcatb.2023.123324.
[15] F. Wang, Y. Gao, H. Fu, S. Liu, Y. Wei, P. Wang, C. Zhao, J. Wang, C. Wang, Almost 100% electron transfer regime over Fe-co dual-atom catalyst toward pollutants removal: regulation of peroxymonosulfate adsorption mode, Appl. Catal. B Environ. Energy 339 (2023), https://doi.org/10.1016/j.apcatb.2023.123178.
[16] B. Li, Y. Liu, K. Hu, Q. Dai, C. Chen, X. Duan, S. Wang, Y. Wang, Spin-regulated Fenton-like catalysis for nonradical oxidation over metal oxide@carbon composites, Adv. Funct. Mater. 34 (2024), https://doi.org/10.1002/adfm.202401397.
[17] C. Zhu, F. Cun, Y. Nie, Q. Du, F. Lao, C. Yue, F. Liu, A. Li, Breaking scaling relation of single-atom site via energy storage-release effect from adjacent carbon vacancy for low-temperature-resistant Fenton-like catalysis, Appl. Catal. B Environ. Energy 358 (2024), https://doi.org/10.1016/j.apcatb.2024.124409.
[18] Z. Yao, Y. Chen, X. Wang, K. Hu, S. Ren, J. Zhang, Z. Song, N. Ren, X. Duan, High-entropy alloys catalyzing polymeric transformation of water pollutants with remarkably improved electron utilization efficiency, Nat. Commun. 16 (2025), https://doi.org/10.1038/s41467-024-55627-7.
[19] J. Wang, S. Wang, Reactive species in advanced oxidation processes: formation, identification and reaction mechanism, Chem. Eng. J. 401 (2020) 126158, https://doi.org/10.1016/j.cej.2020.126158.
[20] S. Xiao, M. Cheng, H. Zhong, Z. Liu, Y. Liu, X. Yang, Q. Liang, Iron-mediated activation of persulfate and peroxymonosulfate in both homogeneous and heterogeneous ways: a review, Chem. Eng. J. 384 (2020), https://doi.org/10.1016/j.cej.2019.123265.
[21] X. Li, X. Liu, L. Xu, Y. Wen, J. Ma, Z. Wu, Highly dispersed Pd/PdO/Fe_2O_3 nanoparticles in SBA-15 for Fenton-like processes: confinement and synergistic effects, Appl. Catal. B Environ. Energy 165 (2015) 79–86, https://doi.org/10.1016/j.apcatb.2014.09.071.
[22] H. Zhang, J. Han, X. Zhang, P. Guo, D. Xie, G. Sheng, Undiscovered multiple roles of multivalent cations in the pollutant removal from actual water by persulfate activated by carbon materials, ACS ES&T Eng. 1 (2021) 1227–1235, https://doi.org/10.1021/acsestengg.1c00121.

[23] L. He, C. Yang, J. Ding, M. Lu, C. Chen, G. Wang, J. Jiang, L. Ding, G. Liu, N. Ren, S. Yang, Fe, N-doped carbonaceous catalyst activating periodate for micropollutant removal: significant role of electron transfer, Appl. Catal. B Environ. Energy 303 (2022) 120880, https://doi.org/10.1016/j.apcatb.2021.120880.
[24] Y. Meng, Y. Liu, C. Wang, Y. Si, Y. Wang, W. Xia, T. Liu, X. Cao, Z. Guo, J. Chen, W. Li, Nanoconfinement steers nonradical pathway transition in single atom Fenton-like catalysis for improving oxidant utilization, Nat. Commun. 15 (2024) 5314, https://doi.org/10.1038/s41467-024-49605-2.
[25] J. Cai, B. Niu, H. Zhao, G. Zhao, Selective Photoelectrocatalytic removal for group-targets of phthalic esters, Environ. Sci. Technol. 55 (2021) 2618–2627, https://doi.org/10.1021/acs.est.0c07106.
[26] Y. Zhen, S. Zhu, Z. Sun, Y. Tian, Z. Li, C. Yang, J. Ma, Identifying the persistent free radicals (PFRs) formed as crucial metastable intermediates during Peroxymonosulfate (PMS) activation by N-doped carbonaceous materials, Environ. Sci. Technol. 55 (2021) 9293–9304, https://doi.org/10.1021/acs.est.1c01974.
[27] L. Cheng, J. Liu, Y. Zhao, Z. Lu, H. Liang, H. Fu, C. Zhen, Z. Ni, R. Zhu, X. Chen, Y. Zhu, R. Qiu, Modulating interfacial electron transfer in hydrothermal carbon/humboldtine to achieve superior heterogeneous Fenton reactivity and H2O2 utilization efficiency, Sep. Purif. Technol. 362 (2025) 131665, https://doi.org/10.1016/j.seppur.2025.131665.
[28] S. Sun, P. Cao, S. Chen, H. Yu, Y. Su, X. Sha, Z. Wang, X. Quan, Oxygen-doped carbon nanospheres embedded with Fe_2C nanoparticles as heterogeneous electro-Fenton catalyst for efficient hydroxyl radical production, Appl. Catal. B Environ. Energy 381 (2026), https://doi.org/10.1016/j.apcatb.2025.125854.
[29] F. Chen, X. Wu, L. Yang, C. Chen, H. Lin, J. Chen, Efficient degradation and mineralization of antibiotics via heterogeneous activation of peroxymonosulfate by using graphene supported single-atom Cu catalyst, Chem. Eng. J. 394 (2020), https://doi.org/10.1016/j.cej.2020.124904.
[30] Y.J. Yao, Z.S. Ma, Z.W. Ma, S.Y. Wang, L.J. Zhang, Y.Y. Wang, S.B. Wang, Dual single atomic Fe-Ni sites in N - doped nanoporous carbon for high-efficiency potassium periodate activation toward pollutant abatement, Sep. Purif. Technol. 353 (2025), https://doi.org/10.1016/j.seppur.2024.128091.
[31] H. Liu, Q. Jin, L. Meng, H. Gu, X. Liang, Y. Fan, Z. Li, F. Zhang, H. Rong, J. Zhang, Cu-based catalysts with the co-existence of single atoms and nanoparticles for basic electrocatalytic oxygen reduction reaction, Nanoscale 15 (2023) 13459–13465, https://doi.org/10.1039/d3nr01810e.
[32] H. Zhang, Y. Zhao, H. Li, J. Wang, Y. Yu, The synergistic effect of co atomic clusters and single atoms facilitates the Fenton-like reaction on A- and R-TiO_2, J. Clean. Prod. 482 (2024) 144194, https://doi.org/10.1016/j.jclepro.2024.144194.
[33] Z. Yang, K. Jiang, G. Tong, C. Ke, H. Wu, P. Liu, J. Zhang, H. Ji, J. Zhu, C. Lu, X. Zhuang, Copper-involved highly efficient oxygen reduction reaction in both alkaline and acidic media, Chem. Eng. J. 437 (2022) 135377, https://doi.org/10.1016/j.cej.2022.135377.
[34] Y. Cheng, H. Wu, J. Han, S. Zhong, S. Huang, S. Chu, S. Song, K.M. Reddy, X. Wang, S. Wu, X. Zhuang, I. Johnson, P. Liu, M. Chen, Atomic Ni and cu co-anchored 3D nanoporous graphene as an efficient oxygen reduction electrocatalyst for zinc-air batteries, Nanoscale 13 (2021) 10862–10870, https://doi.org/10.1039/d1nr01612a.
[35] H. Zhang, C. Li, L. Lyu, C. Hu, Surface oxygen vacancy inducing peroxymonosulfate activation through electron donation of pollutants over cobalt-zinc ferrite for water purification, Appl. Catal. B Environ. Energy 270 (2020), https://doi.org/10.1016/j.apcatb.2020.118874.
[36] H. Shang, X. Zhou, J. Dong, A. Li, X. Zhao, Q. Liu, Y. Lin, J. Pei, Z. Li, Z. Jiang, D. Zhou, L. Zheng, Y. Wang, J. Zhou, Z. Yang, R. Cao, R. Sarangi, T. Sun, X. Yang, X. Zheng, W. Yan, Z. Zhuang, J. Li, W. Chen, D. Wang, J. Zhang, Y. Li, Engineering unsymmetrically coordinated cu-S_1N_3 single atom sites with enhanced oxygen reduction activity, Nat. Commun. 11 (2020), https://doi.org/10.1038/s41467-020-16848-8.
[37] J. Pan, X. Wang, X. Yang, C. Guo, Q. Yue, X. Xu, L. Wang, Y. Gao, B. Gao, Insights into the enhanced oxidation of organic micropollutants by single-atom cu catalyst activated peroxydisulfate: valence-dominated nonradical pathway, Appl. Catal. B Environ. Energy 351 (2024), https://doi.org/10.1016/j.apcatb.2024.123997.
[38] L. Zhang, X. Zhou, L. Yang, Y. Xu, T. Liu, R. Ji, Y. Yang, Y. Zhang, J. Chen, Boosting peracetic acid activation with cu single-atom catalysts for sulfamethoxazole abatement: a nonradical pathway and 'double engine' driving mechanism, Appl. Catal. B Environ. Energy 349 (2024), https://doi.org/10.1016/j.apcatb.2024.123897.
[39] J. Du, Y. Zhang, H. Wu, S. Hou, A. Chen, N-doped hollow mesoporous carbon spheres by improved dissolution-capture for supercapacitors, Carbon 156 (2020) 523–528, https://doi.org/10.1016/j.carbon.2019.09.091.
[40] Y. Ma, D. Wu, T. Wang, D. Jia, Nitrogen, phosphorus co-doped carbon obtained from amino acid based resin Xerogel as efficient electrode for supercapacitor, ACS Appl. Energy Mater. 3 (2020) 957–969, https://doi.org/10.1021/acsaem.9b02032.
[41] P. Yang, S. Zuo, F. Zhang, B. Yu, S. Guo, X. Yu, Y. Zhao, J. Zhang, Z. Liu, Carbon nitride-based single-atom cu catalysts for highly efficient carboxylation of alkynes with atmospheric CO_2, Ind. Eng. Chem. Res. 59 (2020) 7327–7335, https://doi.org/10.1021/acs.iecr.0c00547.
[42] J. Zheng, Q. Lin, Y. Liu, Y. Deng, X. Fan, K. Xu, Y. Ma, J. He, Efficient activation of peroxymonosulfate by Fe single-atom: the key role of Fe-pyrrolic nitrogen coordination in generating singlet oxygen and high-valent Fe species, J. Hazard. Mater. 462 (2024) 132753, https://doi.org/10.1016/j.jhazmat.2023.132753.
[43] T. Zhu, Q. Chen, P. Liao, W. Duan, S. Liang, Z. Yan, C. Feng, Single-atom cu catalysts for enhanced Electrocatalytic nitrate reduction with significant alleviation of nitrite production, Small 16 (2020), https://doi.org/10.1002/smll.202004526.
[44] K. An, X. Xu, Mo_2C based electrocatalyst with nitrogen doped three-dimensional mesoporous carbon as matrix, synthesis and HER activity study, Electrochim. Acta 293 (2019) 348–355, https://doi.org/10.1016/j.electacta.2018.10.050.
[45] J. Hou, T. Cao, F. Idrees, C. Cao, A co-sol-emulsion-gel synthesis of tunable and uniform hollow carbon nanospheres with interconnected mesoporous shells, Nanoscale 8 (2016) 451–457, https://doi.org/10.1039/c5nr06279a.
[46] J. Zhang, Y. Sun, J. Zhu, Z. Kou, P. Hu, L. Liu, S. Li, S. Mu, Y. Huang, Defect and pyridinic nitrogen engineering of carbon-based metal-free nanomaterial toward oxygen reduction, Nano Energy 52 (2018) 307–314, https://doi.org/10.1016/j.nanoen.2018.08.003.
[47] J. Zheng, Q. Lin, Y. Wu, Y. Liu, C. Zeng, Y. Luo, T. Chen, Key coordination of oxygen doping in Fe single-atoms enhances nonradical activation of peroxymonosulfate: the formation of high-valent Fe species and electron transfer, Chem. Eng. J. 489 (2024) 151307, https://doi.org/10.1016/j.cej.2024.151307.
[48] G. Zhou, Y. Chen, G. Chen, H. Xu, W. Yin, B. Wang, X. Zhu, X. Ning, P.K. Chu, X. Wang, H. Xu, Enhanced CO_2 photoreduction in pure water systems by surface-reconstructed asymmetric Mn-cu sites, Appl. Catal. B Environ. Energy 361 (2025), https://doi.org/10.1016/j.apcatb.2024.124617.
[49] W. Ren, L. Xiong, X. Yuan, Z. Yu, H. Zhang, X. Duan, S. Wang, Activation of Peroxydisulfate on carbon nanotubes: Electron-transfer mechanism, Environ. Sci. Technol. 53 (2019) 14595–14603, https://doi.org/10.1021/acs.est.9b05475.
[50] G.P. Anipsitakis, D.D. Dionysiou, Radical generation by the interaction of transition metals with common oxidants, Environ. Sci. Technol. 38 (2004) 3705–3712, https://doi.org/10.1021/es035121o.
[51] J. Wang, S. Wang, Activation of persulfate (PS) and peroxymonosulfate (PMS) and application for the degradation of emerging contaminants, Chem. Eng. J. 334 (2018) 1502–1517, https://doi.org/10.1016/j.cej.2017.11.059.
[52] X. Lu, W. Qiu, J. Ma, H. Xu, D. Wang, H. Cheng, W. Zhang, X. He, The overestimated role of singlet oxygen for pollutants degradation in some non-photochemical systems, Chem. Eng. J. 401 (2020) 126128, https://doi.org/10.1016/j.cej.2020.126128.
[53] P. Duan, M. Li, X. Xu, Q. Yue, Y. Gao, B. Gao, Understanding of interfacial molecular interactions and inner-sphere reaction mechanism in heterogeneous Fenton-like catalysis on Mn-N_4 site, Appl. Catal. B Environ. Energy 344 (2024), https://doi.org/10.1016/j.apcatb.2023.123619.
[54] J. He, Y. Wan, W. Zhou, ZIF-8 derived Fe–N coordination moieties anchored carbon nanocubes for efficient peroxymonosulfate activation via non-radical pathways: role of FeNx sites, J. Hazard. Mater. 405 (2021) 124199, https://doi.org/10.1016/j.jhazmat.2020.124199.
[55] Z. Liu, Y. Zhao, X. Cao, C. Tan, S. Wang, C. Song, J. Lai, Z. Wang, M. Song, High metal-loaded sub-nanocluster catalyst enhanced Fenton-like reaction activity for emerging contaminants degradation by generating high-valent copper, Sep. Purif. Technol. 356 (2025) 129794, https://doi.org/10.1016/j.seppur.2024.129794.
[56] S. Sun, C. Shan, Z. Yang, S. Wang, B. Pan, Self-enhanced selective oxidation of phosphonate into phosphate by cu(II)/H_2O_2: performance, mechanism, and validation, Environ. Sci. Technol. 56 (2022) 634–641, https://doi.org/10.1021/acs.est.1c06471.
[57] S. Pang, J. Jiang, J. Ma, Oxidation of sulfoxides and arsenic(III) in corrosion of nanoscale zero valent iron by oxygen: evidence against ferryl ions (Fe(IV)) as active intermediates in Fenton reaction, Environ. Sci. Technol. 45 (2011) 307–312, https://doi.org/10.1021/es102401d.
[58] K.Z. Huang, H. Zhang, Direct Electron-transfer-based Peroxymonosulfate activation by Iron-doped manganese oxide (δ-MnO_2) and the development of galvanic oxidation processes (GOPs), Environ. Sci. Technol. 53 (2019) 12610–12620, https://doi.org/10.1021/acs.est.9b03648.
[59] J. Yu, Q. Fu, H. Yang, G. Ouyang, J. Wang, Z. Hao, Synergistic catalytic organic pollutants degradation and Cr(VI) reduction by carbon nanotubes through an electron-transfer mechanism without external energy or chemical input, ACS ES&T Eng. 2 (2022) 1221–1228, https://doi.org/10.1021/acsestengg.1c00436.
[60] H. Dong, N. Zhao, Q. Xu, Y. Xiao, W. Zhang, R. Qiu, Urea-tailored biochar activated peroxydisulfate for carbazole degradation: An electron transfer process from in-plane to out-of-plane, J. Clean. Prod. 550 (2026) 147913, https://doi.org/10.1016/j.jclepro.2026.147913.
[61] C. Ling, Z. Zhang, T. Dong, C. Zhu, Y. Xue, J. Han, F. Liu, Constructing low-temperature-resistant advanced oxidation process by hollow porous carbon-supported single-atom Fe catalyst for efficient cold-water decontamination: combined kinetic and thermodynamic optimization, Appl. Catal. B Environ. Energy 372 (2025), https://doi.org/10.1016/j.apcatb.2025.125330.
[62] U. Tylus, Q. Jia, K. Strickland, N. Ramaswamy, A. Serov, P. Atanassov, S. Mukerjee, Elucidating oxygen reduction active sites in Pyrolyzed metal-nitrogen coordinated non-precious-metal Electrocatalyst systems, J. Phys. Chem. C 118 (2014) 8999–9008, https://doi.org/10.1021/jp500781v.
[63] X. Zhang, Y.B. Mollamahale, D. Lyu, L. Liang, F. Yu, M. Qing, Y. Du, X. Zhang, Z. Q. Tian, P.K. Shen, Molecular-level design of Fe-N-C catalysts derived from Fe-dual pyridine coordination complexes for highly efficient oxygen reduction, J. Catal. 372 (2019) 245–257, https://doi.org/10.1016/j.jcat.2019.03.003.
[64] M. Luo, H. Zhang, P. Zhou, Z. Xiong, B. Huang, J. Peng, R. Liu, W. Liu, B. Lai, Efficient activation of ferrate(VI) by colloid manganese dioxide: comprehensive elucidation of the surface-promoted mechanism, Water Res. 215 (2022), https://doi.org/10.1016/j.watres.2022.118243.
[65] K. Yin, R. Wu, Y. Shang, D. Chen, Z. Wu, X. Wang, B. Gao, X. Xu, Microenvironment modulation of cobalt single-atom catalysts for boosting both radical oxidation and electron-transfer process in Fenton-like system, Appl. Catal. B Environ. Energy 329 (2023), https://doi.org/10.1016/j.apcatb.2023.122558.
[66] H. Li, J. Lai, Z. Li, L. Wang, Multi-sites electrocatalysis in high-entropy alloys, Adv. Funct. Mater. 31 (2021) 2106715, https://doi.org/10.1002/adfm.202106715.

[67] D. Zhang, H. Zhao, X. Wu, Y. Deng, Z. Wang, Y. Han, H. Li, Y. Shi, X. Chen, S. Li, J. Lai, B. Huang, L. Wang, Multi-site electrocatalysts boost pH-universal nitrogen reduction by high-entropy alloys, Adv. Funct. Mater. 31 (2021) 2006939, https://doi.org/10.1002/adfm.202006939.
[68] K. Yin, Y. Shang, D. Chen, B. Gao, Q. Yue, X. Xu, Redox potentials of pollutants determining the dominate oxidation pathways in manganese single-atom catalyst (Mn-SAC)/peroxymonosulfate system: selective catalytic mechanisms for versatile pollutants, Appl. Catal. B Environ. Energy 338 (2023) 123029, https://doi.org/10.1016/j.apcatb.2023.123029.
[69] H. Zhang, Z. Wang, J. Zhang, K. Dai, Metal-sulfide-based heterojunction photocatalysts: principles, impact, applications, and in-situ characterization, Chin. J. Catal. 49 (2023) 42–67, https://doi.org/10.1016/S1872-2067(23)64444-4.
[70] D. Zhang, Y. Shi, H. Zhao, W. Qi, X. Chen, T. Zhan, S. Li, B. Yang, M. Sun, J. Lai, B. Huang, L. Wang, The facile oil-phase synthesis of a multi-site synergistic high-entropy alloy to promote the alkaline hydrogen evolution reaction, J. Mater. Chem. A 9 (2021) 889–893, https://doi.org/10.1039/D0TA10574K.
[71] H. Li, M. Sun, Y. Pan, J. Xiong, H. Du, Y. Yu, S. Feng, Z. Li, J. Lai, B. Huang, L. Wang, The self-complementary effect through strong orbital coupling in ultrathin high-entropy alloy nanowires boosting pH-universal multifunctional electrocatalysis, Appl. Catal. B Environ. Energy 312 (2022) 121431, https://doi.org/10.1016/j.apcatb.2022.121431.
[72] P. Xie, T. Pu, G. Aranovich, J. Guo, M. Donohue, A. Kulkarni, C. Wang, Bridging adsorption analytics and catalytic kinetics for metal-exchanged zeolites, Nat. Catal. 4 (2021) 144–156, https://doi.org/10.1038/s41929-020-00555-0.
[73] T. Lu, Q. Chen, Independent gradient model based on Hirshfeld partition: a new method for visual study of interactions in chemical systems, J. Comput. Chem. 43 (2022) 539–555, https://doi.org/10.1002/jcc.26812.
[74] H. Zang, Y. Huang, T. Hao, S. Xiao, J. Zhang, H. Li, B. Yan, Fe−modified and N − doped sludge biochar for BPA removal: PI-activated nonradical oxidation coupled with synergistic adsorption, Sep. Purif. Technol. 379 (2025) 135124, https://doi.org/10.1016/j.seppur.2025.135124.
[75] L. Gan, L. Wang, L. Xu, X. Fang, C. Pei, Y. Wu, H. Lu, S. Han, J. Cui, J. Shi, C. Mei, Fe3C-porous carbon derived from Fe2O3 loaded MOF-74(Zn) for the removal of high concentration BPA: the integrations of adsorptive/catalytic synergies and radical/non-radical mechanisms, J. Hazard. Mater. 413 (2021), https://doi.org/10.1016/j.jhazmat.2021.125305.
[76] X. Li, Z. Wang, B. Zhang, A.I. Rykov, M.A. Ahmed, J. Wang, $FexCo_3$-xO_4 nanocages derived from nanoscale metal-organic frameworks for removal of bisphenol a by activation of peroxymonosulfate, Appl. Catal. B Environ. Energy 181 (2016) 788–799, https://doi.org/10.1016/j.apcatb.2015.08.050.
[77] J. Sharma, I.M. Mishra, D.D. Dionysiou, V. Kumar, Oxidative removal of bisphenol a by UV-C/peroxymonosulfate (PMS): kinetics, influence of co-existing chemicals and degradation pathway, Chem. Eng. J. 276 (2015) 193–204, https://doi.org/10.1016/j.cej.2015.04.021.
[78] K. Wang, T. Zhao, N. Ren, S. Ho, Asymmetric defective sites-mediated high-valent cobalt-oxo species in self-suspension aerogel platform for efficient peroxymonosulfate activation, Water Res. 265 (2024) 122304, https://doi.org/10.1016/j.watres.2024.122304.